Homocoupling Defects of a Small Donor Molecule for Organic Photovoltaics: Quantification of the Eutectic State Diagram by Rapid Heat–Cool Differential Scanning Calorimetry

Van den Brande, Niko; Defour, Maxime; Liu, Zhen; Verstappen, Pieter; Nies, Erik; Maes, Wouter; Van Assche, Guy; Van Mele, Bruno

Published in:
Journal of Physical Chemistry C

DOI:
10.1021/acs.jpcc.9b06336

Publication date:
2019

Homocoupling Defects of a Small Donor Molecule for Organic Photovoltaics: Quantification of the Eutectic State Diagram by Rapid Heat-Cool Differential Scanning Calorimetry

Niko Van den Brande[1*], Maxime Defour[1], Zhen Liu[1], Pieter Verstappen[2,3], Erik Nies[4], Wouter Maes[2,3], Guy Van Assche[1], Bruno Van Mele[1]

[1] Physical Chemistry and Polymer Science (FYSC), Vrije Universiteit Brussel (VUB), Pleinlaan 2, 1050 Brussels, Belgium

[2] Design & Synthesis of Organic Semiconductors (DSOS), Institute for Materials Research (IMO-IMOMEC), Hasselt University, Universitaire Campus, Agoralaan 1, 3590 Diepenbeek, Belgium

[3] imec, Associated Laboratory IMOMEC, Wetenschapspark 1, 3590 Diepenbeek, Belgium

[4] Polymer Chemistry and Materials, Department of Chemistry, KU Leuven, Celestijnenlaan 200f, 3001 Leuven, Belgium

[*]Corresponding author

E-mail: npvdbran@vub.be

Abstract

The conjugated small donor molecule p-DTS(FBTTh$_2$)$_2$, leading to efficient bulk heterojunction organic photovoltaic devices with PC$_{71}$BM, shows a eutectic phase behaviour in combination with its homocoupled analogue. Rapid Heat-Cool Differential Scanning Calorimetry (RHC) allows to construct the state diagram based on (i) the endset of melting of p-DTS(FBTTh$_2$)$_2$:homocoupled p-DTS(FBTTh$_2$)$_2$ mixtures of different composition, and (ii) partial integration of the melting trajectory of these mixtures by calculating the fraction of molten pure excess phase as a function of temperature. These quantitative experimental results are supported by a theoretical calculation model based on Schröder-van Laar equations extended with an interaction function representing the interactions between the mixture's components in the liquid state. The eutectic composition around 30 wt% of homocoupled p-DTS(FBTTh$_2$)$_2$

shows the lowest crystallinity (order) of all mixtures together with a maximum loss of photovoltaic efficiency.

1. Introduction

Over the last years, organic photovoltaics (OPV) have received noticeable attention as a complementary or even alternative technology for classical inorganic photovoltaic cells. The use of a thin organic active layer imparts several useful properties, such as solvent processability and flexibility [1,2]. OPV active layers are generally composed of an electron donor and an electron acceptor, creating a heterojunction that is required for excitonic charge generation with organic semiconductors. A bulk heterojunction architecture is often used to maximize the interface where charge generation can take place, formed by a complex phase separation process during the drying of a solution containing both the donor and acceptor [3].

While acceptor materials have been mostly limited to fullerene derivatives, until the recent introduction of high-efficiency non-fullerene acceptors [4,5], donor materials have undergone a steady improvement over the past years. High-efficiency donor materials are based on the alternation of electron rich and electron deficient subunits, yielding low band gap copolymers or small molecules, which leads to a higher photon absorption [2]. Small molecules have several advantages compared to polymers, such as a simpler synthesis and purification process, better batch-to-batch reproducibility and a monodisperse molecular weight [6,7]. The alternation of electron rich and poor units in low band gap polymers or small molecules is, however, not always perfect. Homocoupling defects, altering the properties of the material and the device performance, are sometimes difficult to avoid [8,9,10,11]. Low molar mass commercial PTB7 (Figure S1) batches containing homocoupling defects were seen to limit device performance by decreasing the open-circuit voltage, lowering the hole mobility, increasing recombination, and finally by leading to a different morphology of the active layer [12]. It is, however, difficult to study the exact effects of homocoupling defects in the case of conjugated polymers, because of the presence of a molecular weight distribution. Conjugated small molecules on the other hand have well-defined molecular weights, and are therefore well-suited as model systems for the study of homocoupling defects.

Of particular interest to this work is p-DTS($FBTTh_2$)$_2$ (Figure 1), a conjugated small molecule affording efficient solar cell devices when combined with $PC_{71}BM$ (Figure S1) [13, 14] , in which homocoupling defects can be introduced during synthesis. In earlier work, p-DTS($FBTTh_2$)$_2$ was used as a model system to study the effect of a controlled amount of homocoupling defects (Figure 1) [15]. Introducing homocoupling led to a drastic decrease of device efficiency, mostly due to a lower short-circuit current density (J_{SC}), even for an amount as low as 5 wt% (relative to p-DTS($FBTTh_2$)$_2$) in the p-DTS($FBTTh_2$)$_2$:$PC_{71}BM$ (60:40) active layer [15]. It was speculated that the morphology of the mixtures was highly affected by the presence of the homocoupled molecules, which gives rise to a ternary system. Determining the precise effect of homocoupled donor molecules on the final morphology is complicated by the use of diiodooctane during processing. Transmission electron microscopy (TEM) was applied to several mixtures to shed light on the issue [15]. It was observed that despite a drastic change in device efficiency, only a subtle difference in morphology (smaller crystalline fibre length and width together with a lower fibre density) could be noticed from TEM images of mixtures containing 0 wt% and 20 wt% homocoupling defects.

Preliminary Rapid Heat-Cool (RHC) DSC measurements on mixtures of p-DTS($FBTTh_2$)$_2$ and its homocoupled analogue revealed a behaviour akin to eutectic mixing, where at the eutectic composition both components solidify together at a single temperature. Interestingly, eutectic behaviour was also observed for P3HT:$PC_{61}BM$ mixtures (Figure S1), a previously widespread OPV system based on a polymer electron donor [16,17,18,19]. The choice of RHC was based on previous work, where it was proven to be an excellent thermal analysis technique for the characterization of OPV active layers and their constituents in general [20,21,22], and more specifically for the construction of their state diagrams [17].

In this work, the eutectic behaviour of the p-DTS($FBTTh_2$)$_2$ donor material when combined with its homocoupled analogue is studied in greater detail by advanced thermal analysis (RHC), leading to the construction of a state diagram based on (i) the endset of melting of p-DTS($FBTTh_2$)$_2$:homocoupled p-DTS($FBTTh_2$)$_2$ mixtures of known composition, and (ii) the melting trajectory of these mixtures by calculating the fraction of molten pure excess phase as a function of temperature. These quantitative experimental results are analysed by a theoretical

model based on the Van Laar/Bragg-Williams (VLBW) theory for the liquid phase and the simplest thermodynamic expression for the solid phase [23].

2. Materials and methods

The small molecules p-DTS($FBTTh_2$)$_2$ (MW = 1220 g.mol^{-1}) and homocoupled p-DTS($FBTTh_2$)$_2$, i.e. (p-DTS)$_2$($FBTTh_2$)$_2$ (MW = 1646 g.mol^{-1}), were synthesised as reported in earlier work and the purity of both materials was verified by NMR spectroscopy and mass spectrometry [15]. Their chemical structures are shown in Figure 1.

Thermal analysis was performed using a Rapid Heat-Cool (RHC) DSC, a prototype developed by TA Instruments [17,24,25]. Calibration of temperature and enthalpy was performed at a scanning rate of 500 K.min^{-1} using indium and adamantane standards. Experiments were performed using helium as a purge gas (10 ml.min^{-1}). Dedicated aluminium RHC crucibles were filled with sample masses in the range of 200–250 μg. A first heating was performed in order to remove thermal history. All thermograms shown in this work correspond to the second heating, which was also used for the state diagrams.

XRD measurements were performed with a Bruker D8 diffractometer, equipped with a Göbel mirror and a 1D lynxeye detector. The measurements were carried out at ambient temperature, from $2\Theta = 2° - 30°$ with a step size of $2\Theta = 0.01°$ and a collecting time of 2 seconds.

A fitting of model interaction parameters was performed by a least sum of squares of differences between experimental (RHC) and modelled (extended Schröder-van Laar equations) data for the liquidus of the eutectic state diagram.

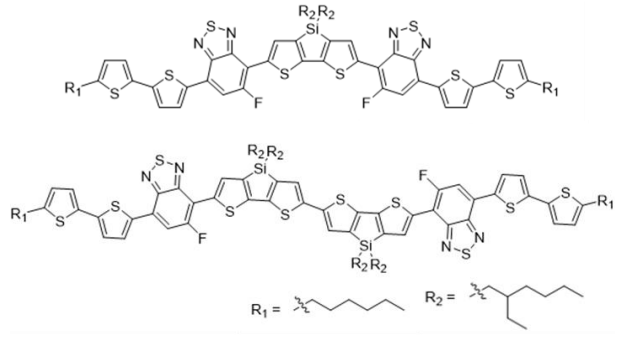

Figure 1: Chemical structure of p-DTS($FBTTh_2$)$_2$ (top) and homocoupled p-DTS($FBTTh_2$)$_2$ or (p-DTS)$_2$($FBTTh_2$)$_2$ (bottom).

3. Results and discussion

3.1. Thermal characterization of p-DTS(FBTTh$_2$)$_2$ and its homocoupled analogue

In order to determine the melting temperature (T_m) as well as the glass transition (T_g), p-DTS(FBTTh$_2$)$_2$ and its homocoupled analogue were subjected to a fast cooling from the melt (at 500 K.min^{-1}) followed by a rapid heating (at 500 K.min^{-1}). Both materials, however, were not quenched to the glassy state under these conditions (results not shown), which illustrates their high crystallisation rate. Therefore, p-DTS(FBTTh$_2$)$_2$ and its homocoupled analogue were subjected to a ballistic cooling in liquid nitrogen from the melt and measured by RHC in a heating step at 500 K.min^{-1}, shown in Figure 2 (left) for p-DTS(FBTTh$_2$)$_2$. It can be seen that although T_g of p-DTS(FBTTh$_2$)$_2$ can be estimated to be between 35 and 50 °C, an accurate determination is impossible due to the rapid onset of cold crystallization after T_g. Under standard heating and cooling rates as employed in DSC or RHC, p-DTS(FBTTh$_2$)$_2$ can thus be considered to be highly crystalline, leading to a sharp and intense melting transition. Similar behaviour is seen for pure homocoupled p-DTS(FBTTh$_2$)$_2$, only in this case the ballistic cooling procedure was not sufficiently fast to allow observation of T_g, indicating that the homocoupled analogue exhibits even faster crystallization kinetics.

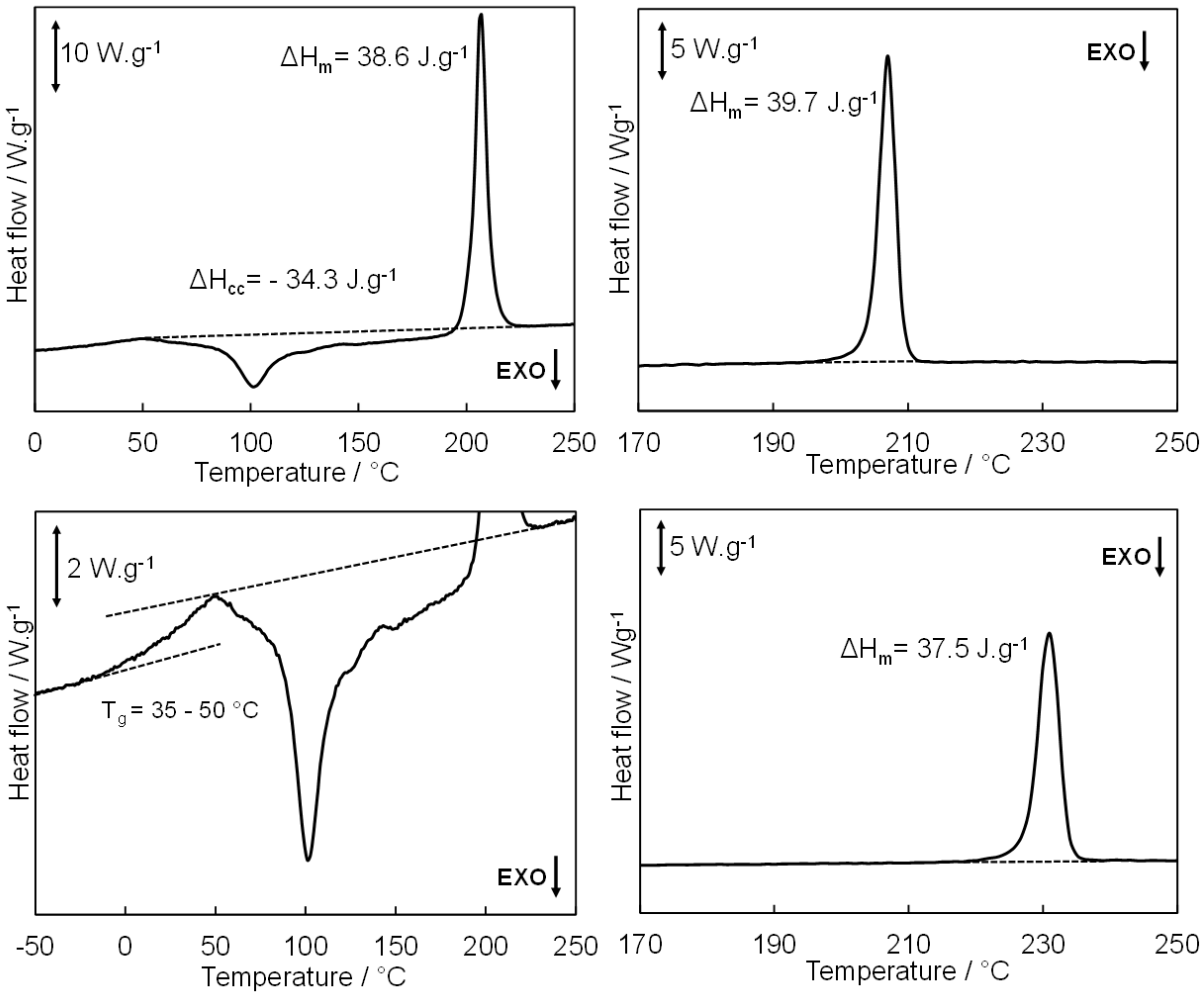

Figure 2: RHC thermograms of pure compounds. Left: (top) Heating curve at 500 K.min^{-1} of p-DTS(FBTTh$_2$)$_2$ after ballistic cooling in liquid nitrogen; (bottom) Magnification of T_g range. Right: Heating curve at 125 K.min^{-1} after cooling at 1 K.min^{-1}: (top) p-DTS(FBTTh$_2$)$_2$; (bottom) Homocoupled p-DTS(FBTTh$_2$)$_2$.

The sharper the peak and the higher the enthalpic content of a material's thermal transition, the easier its detection by RHC (DSC) because of an improved signal-to-noise ratio. This means that p-DTS(FBTTh$_2$)$_2$ and its homocoupled analogue are well-suited for the construction of a state diagram of their binary mixtures by RHC, where the onset and endset of the melting trajectory of a mixture are useful to describe the liquidus and solidus lines and the eventual eutectic. In order to achieve an optimal determination of the state diagram, the following thermal procedure was used: after a first heating to the molten state, slow cooling (1 K.min^{-1}) was applied to allow structure formation by crystallisation, followed by a relatively high heating rate (125 K.min^{-1}) to

melt all crystals. As mentioned before, p-DTS($FBTTh_2$)$_2$ and homocoupled p-DTS($FBTTh_2$)$_2$ were found to crystallize rapidly to a high degree of crystallinity. Moreover, they undergo no reordering when rapidly heated after a slow cooling. A heating rate of 125 K.min^{-1} was preferred over faster rates to avoid excessive peak broadening due to thermal lag. The melting endotherms obtained by following this procedure can be seen in Figure 2 (right). As expected, no T_g and cold crystallization can be observed using this thermal protocol. RHC allows to clearly differentiate the two molecules' melting behaviour since the melting peak temperature of homocoupled p-DTS($FBTTh_2$)$_2$ is at least 20 °C higher and no peak overlap occurs.

3.2. State diagram of p-DTS($FBTTh_2$)$_2$:homocoupled p-DTS($FBTTh_2$)$_2$ mixtures based on endset of melting by RHC

To construct an accurate state diagram by RHC, mixtures of p-DTS($FBTTh_2$)$_2$ and the homocoupled analogue should be characterised. The same thermal procedure as for the pure materials (125 K.min^{-1} heating preceded by 1 K.min^{-1} cooling) was applied to mixtures of different p-DTS($FBTTh_2$)$_2$:homocoupled p-DTS($FBTTh_2$)$_2$ compositions. Figure 3 shows RHC thermograms of the different mixtures. A quantification procedure for the onset and endset values of all melting trajectories is important to construct a reliable state diagram. Calculated temperatures based on melting enthalpy values from 2.5 % (onset temperature T_m^o) to 97.5 % (endset temperature T_m^e) of the melting trajectories are represented in Figure 3, displaying a typical eutectic behaviour. Indeed, upon the addition of homocoupled molecules, the endset T_m^e of the melting trajectory (indicated by closed symbols), corresponding to the liquidus line, first declines towards a minimum value at p-DTS($FBTTh_2$)$_2$:homocoupled p-DTS($FBTTh_2$)$_2$ 70:30 (defined as the eutectic composition *E*, in wt%). The endset of melting at 200 °C for this composition *E* is taken as the eutectic liquidus temperature T_E^e. When the homocoupled p-DTS($FBTTh_2$)$_2$ content is further increased, the endset of melting increases again towards the value of pure homocoupled p-DTS($FBTTh_2$)$_2$. The eutectic melting at *E* between 185 (T_E^o) and 200 (T_E^e) °C is well above the T_g of both compounds (assuming that the homocoupled defect has a similar T_g compared to p-DTS($FBTTh_2$)$_2$) avoiding interference of vitrification of a remaining amorphous phase. On the contrary, P3HT:$PC_{61}BM$ mixtures were mostly amorphous close to the eutectic composition [17]. The low amount or total absence of crystals at *E* was explained by the

increased mixtures' viscosity for high molar mass P3HT in combination with the vitrification of $PC_{61}BM$, whose T_g is close to the onset of melting of P3HT in the eutectic [17]. These conditions do not apply to the p-DTS(FBTTh$_2$)$_2$:homocoupled p-DTS(FBTTh$_2$)$_2$ system, where the constituents have a molar mass orders of magnitude below that of high molar mass P3HT and therefore show a much lower melt viscosity.

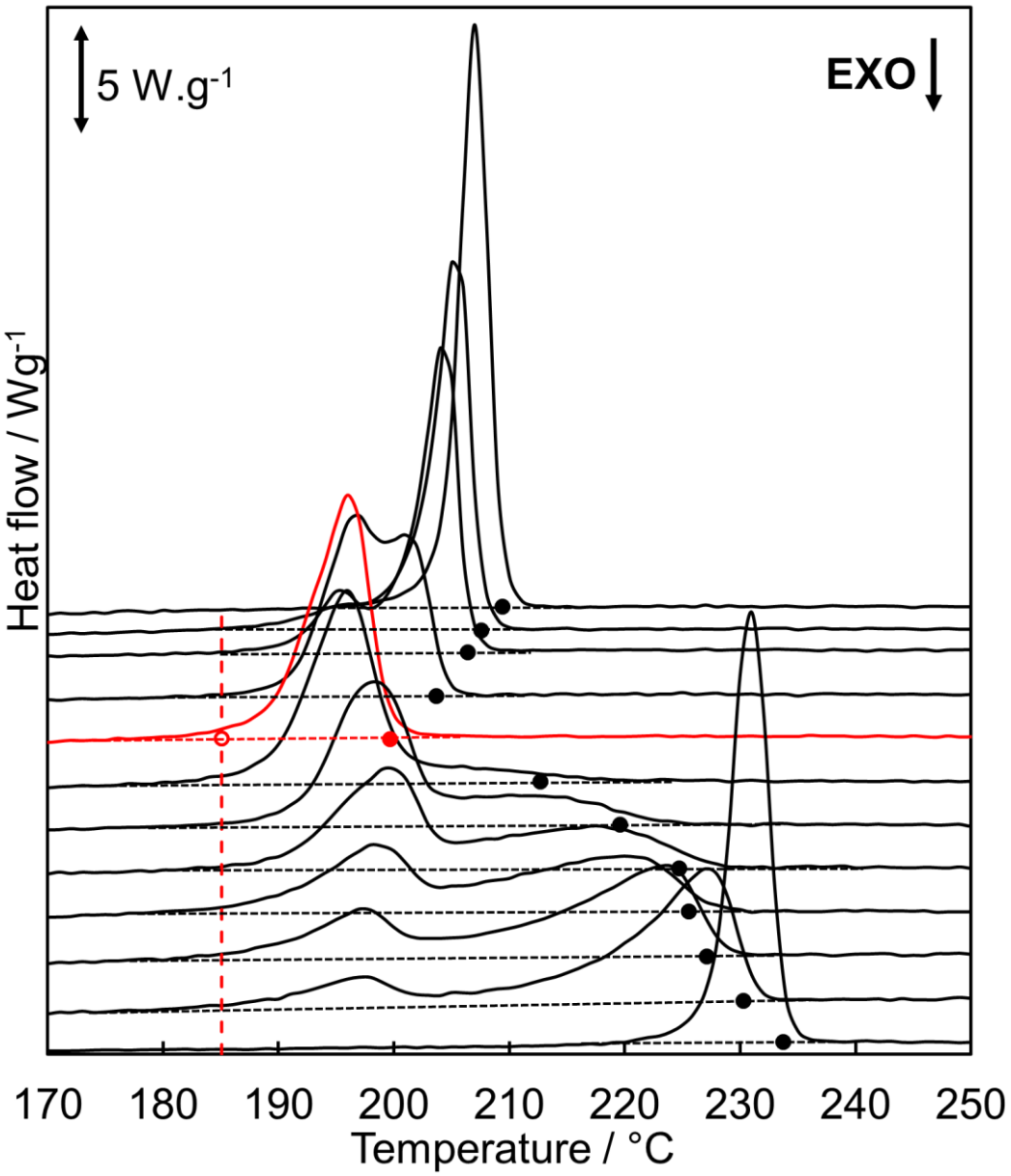

Figure 3: RHC thermograms at 125 K.min^{-1} of p-DTS(FBTTh$_2$)$_2$:homocoupled p-DTS(FBTTh$_2$)$_2$ mixtures of different composition (from top to bottom 100:0, 95:05, 90:10, 80:20, 70:30, 60:40, 50:50, 40:60, 30:70, 20:80, 10:90, 0:100) after slow cooling (1 K.min^{-1}). The 70:30 thermogram (red) exhibits the lowest endset of melting

and is considered as the best approximation of the eutectic. Curves are vertically shifted proportional to the wt% of homocoupled p-DTS(FBTTh$_2$)$_2$. The onset of melting (open symbol at eutectic and vertical dashed line) and the endset of melting (closed symbols) are indicated.

Figure 3 illustrates the ability to detect a low content of homocoupling in p-DTS(FBTTh$_2$)$_2$ mixtures by means of RHC. All mixtures show a clear melting trajectory for compositions deviating from *E*. As can be seen, a 5 wt% content of homocoupling (95:05 composition) is clearly detected since it leads to a distinctly different melting behaviour with a broader melting trajectory compared to pure p-DTS(FBTTh$_2$)$_2$, with a decrease in T_m^e as well as ΔH_m^{95} (see Table 1).

Figure 4 shows the evolution of the endset of melting T^e with composition and is representing the liquidus line of the eutectic state diagram of p-DTS(FBTTh$_2$)$_2$:homocoupled p-DTS(FBTTh$_2$)$_2$. The onset of melting T_E^o for compositions close to *E* is also indicated (open symbol, see also Figure 3), showing the lower temperature limit of the solidus line in equilibrium with the liquidus line. As indicated, a quantification procedure for the onset and endset values of all melting trajectories is important for a reliable state diagram. Experimental (calculated) onset and endset values based on 95% of ΔH_m of all melting trajectories (from 2.5 % to 97.5 %) are represented in Figure 4. The evolution of the experimental (calculated) melting enthalpy ΔH_m^{95} as a function of mixture composition is represented in Figure 5. All values are summarized in Table 1.

The homocoupled molecule has a lower specific melting enthalpy ΔH_m but a higher T_m. An explanation would be a lower entropy of melting (ΔS_m). As homocoupled p-DTS(FBTTh$_2$)$_2$ is a molecule with a higher aspect ratio, the melting of its crystals would lead to a relatively smaller gain in entropy compared to the melting of p-DTS(FBTTh$_2$)$_2$ crystals. A relatively larger decrease of ΔS_m than the drop of ΔH_m would explain the higher T_m (calculated as ΔH_m divided by ΔS_m).

Table 1: Thermal properties of p-DTS(FBTTh$_2$)$_2$, homocoupled p-DTS(FBTTh$_2$)$_2$ and their mixtures at a heating rate of 125 K.min^{-1} after cooling at 1 K.min^{-1}.

Material	T_m^o/ °C	T_m^e/ °C	Experimental	Theoretical

p-DTS(FBTTh$_2$)$_2$:homocoupled p-DTS(FBTTh$_2$)$_2$	(onset)	(endset)	ΔH_m^{95}/ J.g^{-1}	ΔH_m^{95}/ J.g^{-1}
100:0	202	209	39.7	39.7
95:5	193	208	36.2	38.6
90:10	192	206	34.0	37.5
80:20	190	204	35.5	35.3
70:30	185	200	33.1	33.1
60:40	185	213	33.7	33.7
50:50	190	220	34.6	34.4
40:60	190	225	33.9	35.0
30:70	187	226	34.6	35.6
20:80	189	227	35.3	36.2
10:90	188	230	37.9	36.9
0:100	225	234	37.5	37.5

The state diagram can be used as a sensitive tool for the detection of homocoupling in pure p-DTS(FBTTh$_2$)$_2$. Indeed, it is possible to quantify the presence of homocoupled defects for batches with an unknown purity by comparing the endset of melting with the values indicated in the state diagram. If this holds for less well-defined systems sensitive to homocoupling defects, such as low bandgap donor copolymers, the construction of state diagrams through RHC could be of added value for the detection of these defects, especially in the resulting mixtures of donor and acceptor material. For example, it was seen that the conventionally used technique of TEM could not distinguish between mixtures with 20 wt% of homocoupled defects and homocoupling-free mixtures [15].

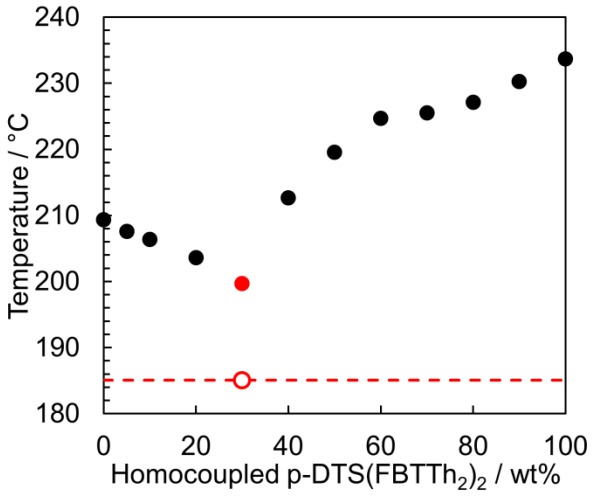

Figure 4: State diagram of p-DTS(FBTTh$_2$)$_2$:homocoupled p-DTS(FBTTh$_2$)$_2$, corresponding to the RHC thermograms of Figure 3, represented by the endset of the melting trajectory of each mixture (liquidus line, closed symbols) with indication of the onset of melting of the eutectic (red open symbol + dashed horizontal line).

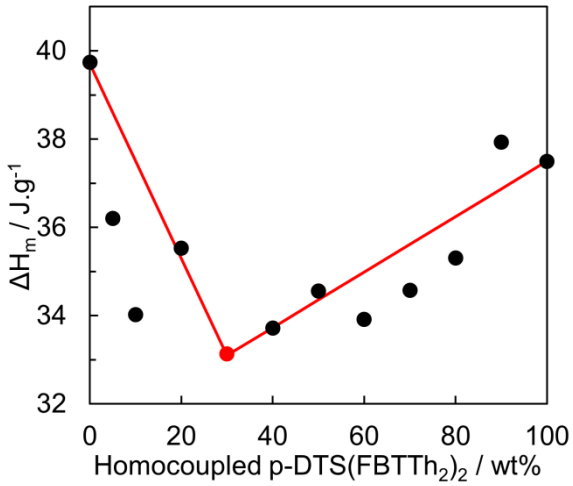

Figure 5: Experimental melting enthalpy ΔH_m^{95} (closed symbols) of p-DTS(FBTTh$_2$)$_2$:homocoupled p-DTS(FBTTh$_2$)$_2$ mixtures as a function of composition measured with RHC at 125 K.min^{-1} after slow cooling at 1 K.min^{-1} and theoretical prediction based on Eq. (3) (red lines).

3.3. Alternative approach for the state diagram of p-DTS(FBTTh$_2$)$_2$:homocoupled p-DTS(FBTTh$_2$)$_2$ mixtures

The state diagram presented above (Figure 4) was constructed by plotting for different samples the endset of the melting trajectory as a function of mixture composition. The underlying rationale is that the endset of the melting peak trajectory corresponds to the liquidus line since the mixture is entirely liquid above this temperature. As RHC is a quantitative calorimetric technique allowing to measure ΔH_m of an endothermic transition, it is possible to quantify the fraction of crystals melting in a certain temperature window of the melting trajectory. In the case of two compounds displaying a *simple* eutectic behaviour with a three-phase equilibrium between two pure crystalline phases and a mixed liquid phase of concentration *E* in a temperature region between the onset T_E^o and endset T_E^e of the eutectic melting transition, the quantitative measurement of the partial ΔH_m for each individual mixture should allow to define the fraction of the molten (pure) excess phase as a function of temperature, as illustrated for a 10:90 p-DTS(FBTTh$_2$)$_2$:homocoupled p-DTS(FBTTh$_2$)$_2$ mixture in Figure 6. The top graph represents the melting trajectory of the 10:90 mixture which is composed of two partly overlapping contributions: (i) the melting transition between the onset T_E^o and endset T_E^e of melting of a fraction with eutectic composition *E*; it is assumed that this eutectic fraction contains 30 wt% of homocoupled p-DTS(FBTTh$_2$)$_2$ with a melting enthalpy $\Delta H_{m,E}$ ($\Delta H_{m,E}^{95}$ = 33.1 J.g^{-1}), and (ii) a melting trajectory of a partly overlapping excess fraction of pure homocoupled p-DTS(FBTTh$_2$)$_2$ with a melting enthalpy $\Delta H_{m,B}$ ($\Delta H_{m,B}^{95}$ = 37.5 J.g^{-1}). If the mixture is represented as '*A*:*B*' with *A* wt% of p-DTS(FBTTh$_2$)$_2$ and *B* wt% of homocoupled p-DTS(FBTTh$_2$)$_2$, the calculated amounts of these eutectic and excess fractions in wt% are:

Eutectic fraction (wt%): $A + (E/(100 - E)).A = [(100 - B)/(100 - E)].100$ (1)

and

Excess fraction *B* (wt%): $B - (E/(100 - E)).A = [(B - E)/(100 - E)].100$ (2)

The theoretical total melting enthalpy of the mixture $\Delta H_m(A{:}B)$ is thus the sum of the enthalpic contributions of the eutectic and excess weight fractions:

$$\Delta H_m(A{:}B) = \Delta H_{m,E}.[(100 - B)/(100 - E)] + \Delta H_{m,B}.[(B - E)/(100 - E)] \quad (3)$$

In case of the 10:90 mixture with *E* = 30 wt%, the eutectic and excess fractions are 14.3 wt% and 85.7 wt% with enthalpic contributions of 4.7 J.g^{-1} and 32.1 J.g^{-1}, respectively. By partial

integration of the melting curve for the 10:90 mixture backward from the highest temperature T_{90}^e to lower temperatures T_x^e, ending at T_E^e (see Figure 6), the partial $\Delta H_m(T_{90}^e \rightarrow T_x^e)$ values allow to calculate the liquidus line of the excess phase (ii) in the state diagram according to:

$$C_x = B - [\Delta H_m(T_{90}^e \rightarrow T_x^e)/\Delta H_{m,B}].(100 - E) \quad (4)$$

with C_x the wt% of homocoupled p-DTS$(FBTTh_2)_2$ between C_{90} (B = 90) and C_E (E = 30) in the bottom graph of Figure 6, corresponding to the temperature T_x^e between T_{90}^e and T_E^e in the upper graph of Figure 6. The fraction of molten pure excess phase (ii) at T_x^e is accordingly calculated as:

$$(C_x - E)/(B - E) \quad (5)$$

Note that the partial enthalpy contribution related to the melting of the eutectic crystals should not lead to an increase of the melting temperature. Only the partial enthalpy contributions of the melting of pure crystals of homocoupled p-DTS$(FBTTh_2)_2$ in the excess phase should lead to an increase of the melting temperature T_x^e, starting from T_E^e till the temperature T_{90}^e of the liquidus at the final 10:90 composition (Figure 6, bottom graph). Note also that between 185 °C (T_E^o) and 200 °C (T_E^e) it is not possible to consider the two melting processes (i) and (ii) separately since both eutectic crystals and the crystals of the excess phase should start melting from T_E^o. The contribution of melting of eutectic phase between T_E^o and T_E^e should be taken into account as a small correction at the end of the backward partial integration of $\Delta H_m(T_{90}^e \rightarrow T_x^e)$ of pure excess phase (ii). The bottom graph of Figure 6 resembles the right side of the eutectic state diagram of Figure 4 although the approach is different. Figure 6 gives more insight in the melting process of one specific mixture by presenting the evolution of the fraction of molten pure excess phase as a function of temperature, while Figure 4 is constructed using endset temperatures of melting for samples of different composition.

There is a clear relationship between the trajectory of the melting curve and the shape of the liquidus line of an excess phase. Beyond T_E^e, the slope of the onset of the melting trajectory of the pure excess phase (homocoupled p-DTS$(FBTTh_2)_2$) is almost flat. Consequently, the amount of molten crystals is hardly increasing for an important increase of temperature. However, from 215 °C on the slope of the melting curve is increasing significantly, and the corresponding liquidus line is flattening off above 45 wt%. So, the lower the slope of the melting trajectory the

steeper the liquidus line, and *vice versa* (Figure 6, top graph beyond T_E^e compared to bottom graph beyond 30 wt%).

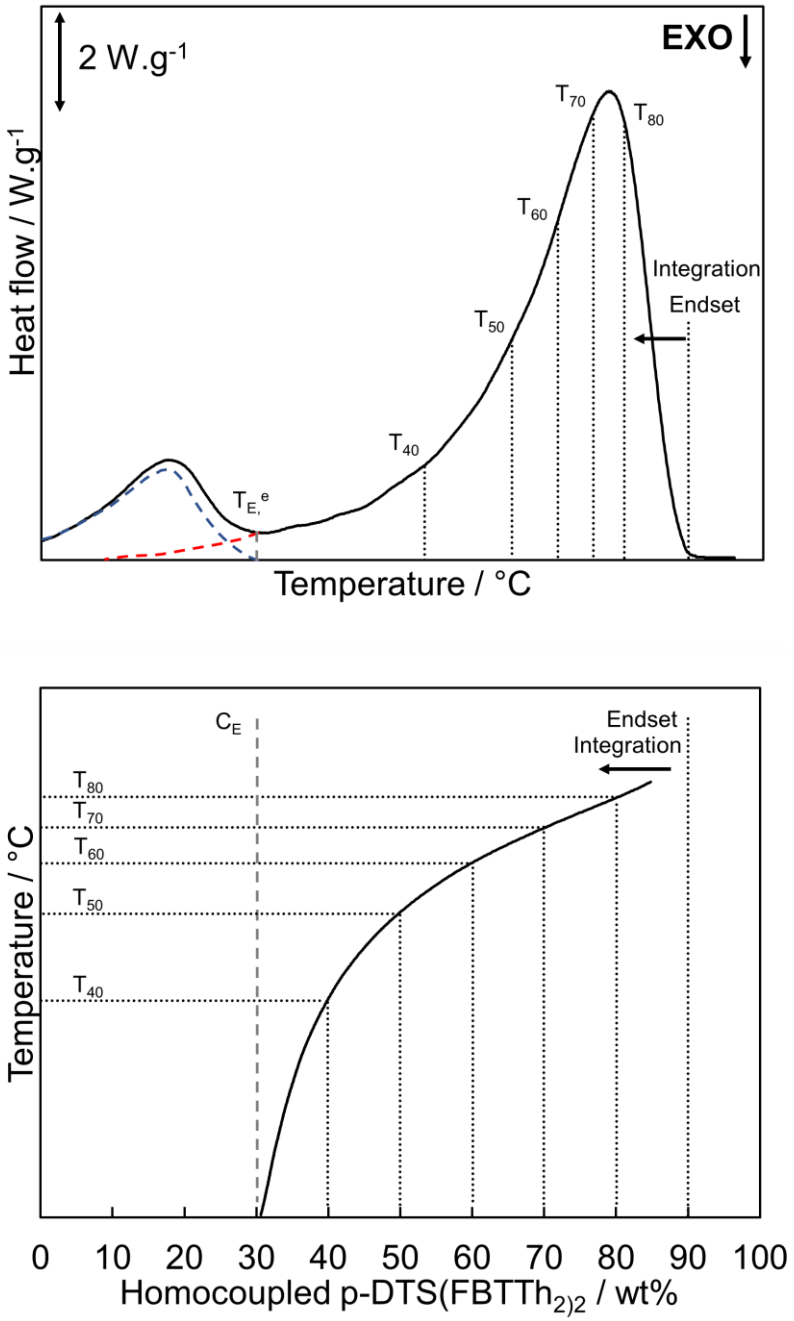

Figure 6: (top) RHC heat flow of melting trajectory of p-DTS(FBTTh$_2$)$_2$:homocoupled p-DTS(FBTTh$_2$)$_2$ A:B (10:90) mixture which contains an excess of B compared to *E* (containing 30 wt% of B). The blue dashed curve represents the melting peak of the eutectic crystals (see Eqs. 1 and 3), the red dashed curve the melting trajectory of the pure excess phase B (see Eqs. 2 and 3). The grey dashed vertical line is the temperature at which the melting of the eutectic crystals is completed (T_E^e). Vertical dotted lines represent selected melting temperatures T_x for backward partial integration of the melting curve. (bottom) Evolution of the selected temperatures T_x as a function of C_x (wt% of pure excess phase B).

This alternative approach based on partial integration can be applied to other p-DTS(FBTTh$_2$)$_2$:homocoupled p-DTS(FBTTh$_2$)$_2$ mixtures, e.g. a 95:05 mixture at the left side of the eutectic with a pure excess phase of *A* in this case, using similar equations:

Eutectic fraction (wt%): $B + ((100 - E)/E).B = [B/E].100$ (1')

Excess fraction *A* (wt%): $A - ((100 - E)/E).B = [(E - B)/E].100$ (2')

$\Delta H_m(A:B) = \Delta H_{m,E}.[B/E] + \Delta H_{m,A}.[(E - B)/E]$ (3')

$C_y = B + [\Delta H_m(T_{05}^e \rightarrow T_y^e)/\Delta H_{m,A}].E$ (4')

with C_y the wt% of homocoupled p-DTS(FBTTh$_2$)$_2$ between C_{05} (*B* = 05) and C_E (*E* = 30), corresponding to the temperature T_y^e between T_{05}^e and T_E^e. The fraction of molten pure excess phase (ii) at T_y^e is accordingly calculated as:

$(E - C_y)/(E - B)$ (5')

The (backward) partial integration of the melting trajectory of the excess phase of the 95:05 mixture leads to the liquidus line of the excess phase *A* at the left side of the eutectic in the state diagram. Figure 7 shows this calculation procedure for both 95:05 and 10:90 p-DTS(FBTTh$_2$)$_2$:homocoupled p-DTS(FBTTh$_2$)$_2$ mixtures, in comparison with the results based on the endset of melting of the different mixtures of Figure 4. The liquidus lines according to the partial integration of a melting trajectory and based on the endset of melting of different mixtures show a similar shape and lead to a similar state diagram as long as the endset values are chosen with caution. The endset values are most influenced by the tail at the end of the melting trajectories, which is caused by the shape of the liquidus line but also partly by the time lag of the measuring instrument. While the state diagram based on the endset of melting can be shifted to slightly higher temperatures depending on the 'endset criterion', this distortion of the liquidus line can be excluded in the method of partial integration.

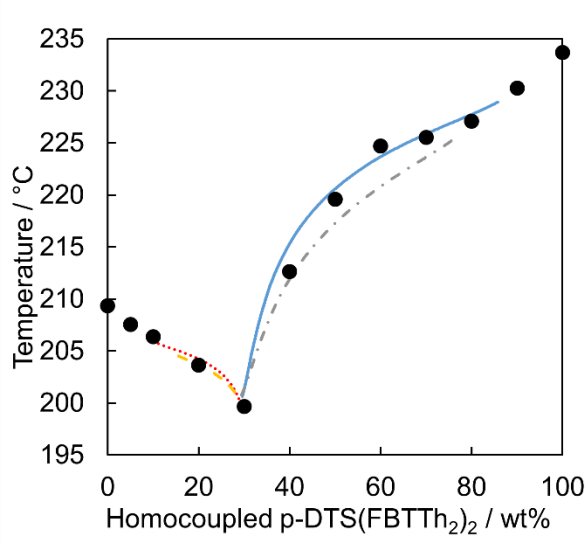

Figure 7: Comparison between state diagram based on endset of melting of each mixture (closed symbols) and state diagram based on partial integrations of p-DTS(FBTTh$_2$)$_2$:homocoupled p-DTS(FBTTh$_2$)$_2$ 95:05 (red dotted line), 90:10 (yellow dashed line), 20:80 (grey dash-dotted line) and 10:90 (blue line).

This alternative approach is applicable to all mixtures with compositions different from the eutectic, as shown in Figure 7 for four compositions describing the excess phase of p-DTS(FBTTh$_2$)$_2$ (95:05 and 90:10) and homocoupled p-DTS(FBTTh$_2$)$_2$ (20:80 and 10:90), respectively. All mixtures show similar trajectories but the results are less accurate for mixtures which are closer to the eutectic composition, probably because of the uncertainty on the exact composition of the eutectic. Indeed, in the equations used, *E* is defined at 30 wt% of homocoupled p-DTS(FBTTh$_2$)$_2$ as it is the mixture displaying the lowest melting point. A slight deviation from 30 wt% for the exact composition of *E* has a relatively more important effect on the calculations for mixtures around *E*. Mixtures closely around *E* are not the best choice anyway, since they just allow the construction of a limited part of the liquidus line.

In conclusion, Figure 7 illustrates that the state diagram can also be developed using this alternative approach, merely based on two mixtures with a composition close to the pure constituent materials, at least if the composition of the eutectic is known. The latter could be estimated by an adequate theoretical model based on extended Schröder-van Laar equations, taking the interactions between the components in the liquid state into account.

3.4. Theoretical model of the p-DTS(FBTTh$_2$)$_2$:homocoupled p-DTS(FBTTh$_2$)$_2$ eutectic state diagram

As it will become clear, the curvature of the state diagram for mixtures enriched in homocoupled p-DTS(FBTTh$_2$)$_2$, as seen in Figure 7, suggests that the interactions between the two constituents in the molten state are more complex than can be expected from typical mixture theories. Therefore, a theoretical model for this non-ideal state diagram is proposed based on the Van Laar/Bragg-Williams (VLBW) theory for the liquid phase extended with an interaction function g arising from the interactions between the mixture's components and the simplest thermodynamic expression for the solid phase [23]:

$$\frac{\Delta H_{m1}^0}{R}\left(\frac{1}{T_{m1}^0}-\frac{1}{T_{m1}}\right) = ln(x_1) + gx_2^2 \quad (6)$$

$$\frac{\Delta H_{m2}^0}{R}\left(\frac{1}{T_{m2}^0}-\frac{1}{T_{m2}}\right) = ln(x_2) + gx_1^2 \quad (7)$$

In these equations the left-hand side represents the excess chemical potentials of component *1* and *2* in the solid phase and the right-hand side the excess chemical potential of the same component in the liquid mixture; indices *1* and *2* refer to p-DTS(FBTTh$_2$)$_2$ and homocoupled p-DTS(FBTTh$_2$)$_2$, respectively; $x_{1,2}$ represent the molar fractions of the components; $\Delta H_{m1,2}^0$ [J.mol^{-1}] the melting enthalpy of the pure components; $T_{m1,2}^0$ [K] the melting temperature of the pure components at equilibrium (as an approximation, the endset value T_m^e at 125 K.min^{-1} after slow cooling at 1 K.min^{-1} was used); $T_{m1,2}$ [K] the melting temperature of the respective excess phases of the mixture; R [J.K^{-1}.mol^{-1}] the gas constant; and g is a dimensionless interaction function.

The eutectic state diagram based on the set of experimental data from (i) the endset of melting of different mixture compositions (see **3.2.**) and/or (ii) the alternative approach by partial integration of the melting trajectory (see **3.3.**) could be used for evaluation of the extended Schröder-van Laar equations (6) and (7) and a meaningful fitting of the interaction function *g*. In the following discussion, a sum of least squares optimization is applied on the smallest experimental data set which is evenly spread over all mixture compositions, i.e. the available data points of the endsets of melting. This limited set of 12 data points provides information on

the pure components, on mixtures with a low content of the second component, as well as on mixtures closer to the eutectic.

If $g = 0$ equations (6) and (7) are the Schröder-van Laar equations describing the melting point depression of a solid in equilibrium with the binary liquid mixture of component *1* and *2* with composition x_2, in the event that the thermodynamic properties of the liquid and solid phases are ideal [26]. The Schröder-van Laar equations describe accurately the experimental data for (almost) ideal conditions, i.e. mixtures with a very low content of 'impurity', but fail to describe the eutectic state diagram for intermediate compositions between 30 and 85 wt%, as can be seen in Figure 8 (dashed curve). The Schröder-van Laar equations predict T_E = 196 °C and C_E = 37 wt% (x_2 is recalculated from molar fraction into wt% homocoupled p-DTS(FBTTh$_2$)$_2$) which are rough estimates and should only be used as a guide (see Figure 8) [23].

A first expression of the interaction function g embodies the excess enthalpy of mixing h as defined by equation (8):

$$g = h/T \tag{8}$$

The excess enthalpy of mixing can be derived from the lattice theory for mixtures of equal-sized spherical molecules. The parameter h is then given by [23]:

$$h = z(\epsilon_{12} - (\epsilon_{11} + \epsilon_{22})/2)/R \tag{9}$$

with z the lattice coordination number and ϵ_{ij} the interaction energy of the ij-pair of nearest neighbours in the lattice. When h is positive (negative) the excess enthalpy of mixing is endothermic (exothermic). The fit of equations (6), (7) and (8) to the experimental data gives $h > 0$ (see Table 2), demonstrating that the mixing of p-DTS(FBTTh$_2$)$_2$ and homocoupled p-DTS(FBTTh$_2$)$_2$ would be clearly endothermic. Although equation (8) overall improves the agreement between theory and experimental data, especially the course of the liquidus at high concentrations of the homocoupled component misses the typical shape of the experimental data (see Figure 8 (dotted curve)).

Equation (8) is known to be too simple to represent real mixtures and often one opts for semi-empirical extensions by making the interaction function g temperature dependent and/or concentration dependent [23]. A number of possible extensions were tested. It was tried for

instance to improve the agreement with experimental data by extending the temperature dependency of g, like $g = a + h/T + b.T + c.\ln(T)$. However, this approach was not successful. As an alternative, the interaction function g was made concentration dependent, introducing an entropic contribution with the extra parameter g_x in equation (10):

$$g = h/T + g_x.x_2 \qquad (10)$$

It represents the simplest extension that was successful in giving a very reasonable description of the experimental results with the use of just one additional fitting parameter, g_x. The fit of equations (6), (7) and (10) (semi-) quantitatively captures the shapes of both liquidus lines and the location of the eutectic (see Figure 8 (full curve)). The enthalpic contribution is reduced more than tenfold in absolute value and is now slightly negative, indicative for exothermic mixing, in combination with an entropic correction g_x governing the fit (see Table 2). The small value of h implies the mixture is close to being *athermal* and the uncertainty on h suggests that it is possible to treat the system as being athermal ($h = 0$) according to equation (11):

$$g = g_x.x_2 \qquad (11)$$

The athermal fit is nearly of the same quality as the fit including the enthalpic parameter h (see Table 2) and is therefore not distinguishable from the full curve in Figure 8. In view of the similarity in chemical structure of both components, shown in Figure 1, it is reasonable that the mixing of both components is close to being athermal. The positive value of $g_x.x_2$ (proportional to $-\frac{T\Delta S}{R}$ in the excess Gibbs energy of mixing) also shows that a *negative* excess entropy ΔS is needed to describe the data. Thus, the conventional combinatorial/translational entropy of mixing does not cover all entropy effects in the system and another entropic effect, accounted for by $g_x.x_2$, is important in the mixture. Since both molecules are clearly not simple spherical molecules (leading to the ideal entropy of mixing in equations (6) and (7)) but are elongated more rod-like molecules, orientational entropy effects will play a role.

It is clear that a much better description of the eutectic state diagram is obtained if the interaction parameter $g \neq 0$. The results of the consecutive optimization steps are summarized in Table 2 and shown in Figure 8. The best fit is obtained by using both fitting parameters h and g_x leading to a

eutectic at C_E = 29.7 wt% and T_E = 200.2 °C. Moreover, in case of athermal mixing a fit of similar quality is obtained.

Despite the important improvement given by equation (10) the model is not yet quantitative in the full composition range and sizeable deviations between 60 - 80 wt% of homocoupled p-DTS(FBTTh$_2$)$_2$ remain. Evidently, the simple entropic correction g_x is only a first order estimate of the supposed orientation entropy effect in the liquid mixture. To proceed further a more detailed model for the liquid state should be used, taking into account the orientational entropy of the two components and their mutual influence in the mixture, as well as the additional enthalpic effects arising from the energetic interactions between these non-spherical molecules. In fact the small $h < 0$ value could indicate that favourable interactions between p-DTS(FBTTh$_2$)$_2$ and homocoupled p-DTS(FBTTh$_2$)$_2$ exist. This is well conceivable in view of possible $\pi - \pi$ stacking interactions between parallel aligned molecules of both components.

Table 2: Fitting results of extended Schröder-van Laar model based on endsets of melting (12 data points).

Model	h / K	g_x	C_E / wt%	T_E / K	Least sum of squares
Schröder-van Laar	-	-	37.0	195.5	-
g = h/T	472 +/- 52	-	25.2	202.1	93.3
g = h/T + $g_x.x_2$	-22 +/- 47	3.09 +/- 0.28	29.7	200.2	7.97
g = $g_x.x_2$	-	2.96 +/- 0.09	29.5	200.3	8.13

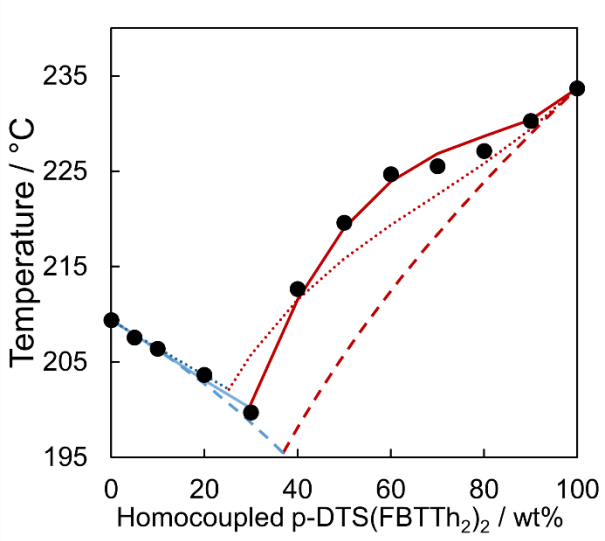

Figure 8: Experimental and modelled state diagram of p-DTS(FBTTh$_2$)$_2$:homocoupled p-DTS(FBTTh$_2$)$_2$. Experimental endset of the melting trajectory of each mixture (closed symbols); Schröder-van Laar equations (dashed curves); extended Schröder-van Laar model with only enthalpic interactions (dotted curves); extended Schröder-van Laar model with enthalpic and entropic interactions (full curves) [23]. For C_E and T_E values see Table 2.

3.5. Importance of the eutectic composition for OPV cell efficiency

It is noteworthy that the p-DTS(FBTTh$_2$)$_2$:PC$_{71}$BM OPV devices with the lowest efficiency in our previous study possessed an amount of homocoupled donor in close vicinity of the eutectic composition of p-DTS(FBTTh$_2$)$_2$:homocoupled p-DTS(FBTTh$_2$)$_2$ mixtures (see Figure 9) [15].

Indeed, the poorest device efficiency was observed when 20 wt% of the homocoupled material was used relative to p-DTS(FBTTh$_2$)$_2$, which is close to *E* estimated at 30 wt% homocoupled p-DTS(FBTTh$_2$)$_2$. Moreover, it cannot be excluded that the lowest efficiency is even closer to 30 wt% of homocoupled p-DTS(FBTTh$_2$)$_2$. The lower efficiency of devices upon the addition of homocoupling defects could partly be explained by the lower crystallinity observed if *E* is approached [15]. Figure 9 shows that the melting enthalpy declines towards a minimum around *E* (decrease of 17% against melting enthalpy of pure p-DTS(FBTTh$_2$)$_2$).

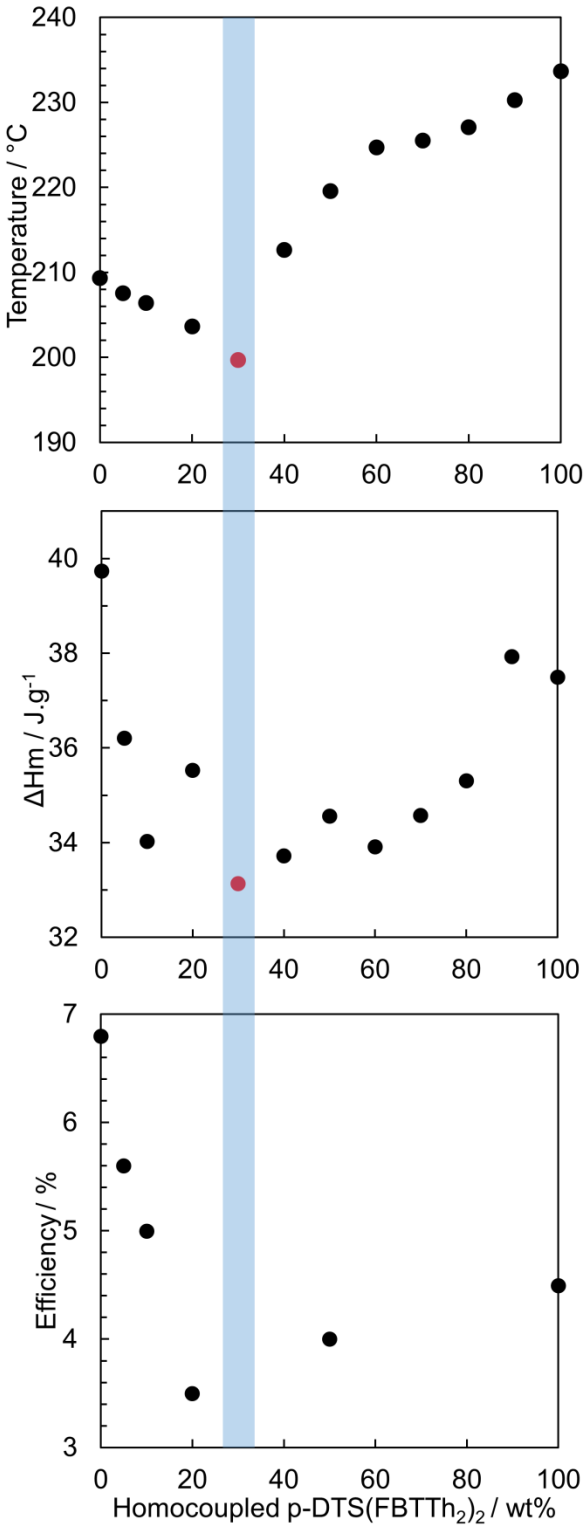

Figure 9: Endset of the melting trajectory (top), and ΔH_m^{95} (middle) of p-DTS(FBTTh$_2$)$_2$:homocoupled p-DTS(FBTTh$_2$)$_2$ mixtures measured with RHC at 125 K.min^{-1} after slow cooling at 1 K.min^{-1}. Efficiency of OPV devices with a donor/acceptor 60:40 active layer, made of PC$_{71}$BM as acceptor and p-DTS(FBTTh$_2$)$_2$:homocoupled p-DTS(FBTTh$_2$)$_2$ mixtures as donor (bottom) [15].

The lower $\Delta H_{m,E}$ (and therefore mixture's crystallinity) is most probably caused by the less perfect crystals formed in eutectic conditions. The lower crystallinity around C_E is supported by comparing the x-ray diffraction (XRD) peaks of the pristine materials with the ones of a eutectic mixture (see Figure 10). This figure shows that both pure materials display more intense and sharp peaks compared to the eutectic mixture. Note again that no vitrification effect and no glass transition temperature are observed around *E*. It should however be pointed out that conclusions from the melting enthalpies of bulk mixtures, as measured in this study, cannot simply be extrapolated towards thin layers used in actual devices, as in the latter surface effects between active layer and electrodes may play a crucial role.

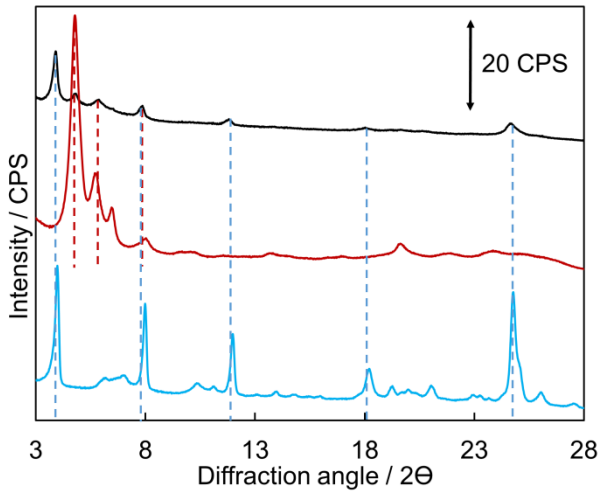

Figure 10: X-ray diffractograms of p-DTS(FBTTh$_2$)$_2$ (100:0, blue curve), homocoupled p-DTS(FBTTh$_2$)$_2$ (0:100, red curve) and the eutectic mixture (70:30, black curve).

4. Conclusions

RHC was introduced as a dedicated thermal analysis technique to construct the state diagram of p-DTS(FBTTh$_2$)$_2$:homocoupled p-DTS(FBTTh$_2$)$_2$, a system which corresponds to a high-efficiency OPV small molecule electron donor material with homocoupling defects. This was achieved by the analysis of p-DTS(FBTTh$_2$)$_2$ mixtures with a known fraction of homocoupled p-DTS(FBTTh$_2$)$_2$. Using slow cooling at 1 K.min^{-1} followed by fast heating at 125 K.min^{-1}, the pristine materials and their mixtures exhibited a clear melting behaviour, with no observable T_g nor cold crystallisation. The liquidus line based on the endset temperature of melting of mixtures of different composition revealed a typical eutectic state diagram, with a eutectic concentration

C_E around 30 wt% homocoupled p-DTS($FBTTh_2$)$_2$. An alternative quantitative approach based on the partial integration of melting trajectories of mixtures displaying a eutectic was introduced. This allowed to get a better insight in the evolution of temperature as a function of the relative fraction of molten pure excess phase of both p-DTS($FBTTh_2$)$_2$ and homocoupled p-DTS($FBTTh_2$)$_2$.

These quantitative experimental data were supported by theoretical calculations, based on extended Schröder-van Laar equations with an interaction function for composition dependent interactions between the two components in the liquid state. Entropic effects are dominant and the mixture almost behaves as a pure *athermal* system.

Moreover, the melting enthalpy of the mixtures and therefore their degree of crystallinity and order declined when approaching C_E and reached a minimum at that very composition. Since OPV devices with an active layer made of $PC_{71}BM$ as acceptor and p-DTS($FBTTh_2$)$_2$:homocoupled p-DTS($FBTTh_2$)$_2$ mixtures as donor showed the lowest efficiency in close vicinity of the donor mixture's eutectic, this reduced order could be a major reason for the observed loss of device efficiency.

Supporting information

Chemical structures of donor and acceptor materials mentioned in introduction.

Acknowledgements

The authors thank the Research Foundation – Flanders (FWO-Vlaanderen) for financial support (project G082718N and postdoctoral fellowship P.V.). The XRD measurements were performed by Bart Ruttens in the group of Prof. Jan D'Haen at Hasselt University.

5. References

(1) Brabec, C. J.; Gowrisanker, S.; Halls, J. J. M.; Laird, D.; Jia, S.; Williams, S. P. Polymer-Fullerene Bulk-Heterojunction Solar Cells. *Adv. Mater.* **2010**, *22*, 3839–3856.

(2) Etxebarria, I.; Ajuria, J.; Pacios, R. Solution-Processable Polymeric Solar Cells: A Review on Materials, Strategies and Cell Architectures to Overcome 10%. *Org. Electron.* **2015**, *19*, 34–60.

(3) Huang, Y.; Kramer, E. J.; Heeger, A. J.; Bazan, G. C. Bulk Heterojunction Solar Cells:

Morphology and Performance Relationships. *Chem. Rev.* **2014**, *114*, 7006–7043.

(4) Bin, H.; Gao, L.; Zhang, Z.-G.; Yang, Y.; Zhang, Y.; Zhang, C.; Chen, S.; Xue, L.; Yang, C.; Xiao, M.; et al. 11.4% Efficiency Non-Fullerene Polymer Solar Cells with Trialkylsilyl Substituted 2D-Conjugated Polymer as Donor. *Nat. Commun.* **2016**, *7*, 13651.

(5) Zhang, G.; Zhao, J.; Chow, P. C. Y.; Jiang, K.; Zhang, J.; Zhu, Z.; Zhang, J.; Huang, F.; Yan, H. Nonfullerene Acceptor Molecules for Bulk Heterojunction Organic Solar Cells. *Chem. Rev.* **2018**, *118*, 3447–3507.

(6) van der Poll, T. S.; Love, J. A.; Nguyen, T.-Q.; Bazan, G. C. Non-Basic High-Performance Molecules for Solution-Processed Organic Solar Cells. *Adv. Mater.* **2012**, *24*, 3646–3649.

(7) Kyaw, A. K. K.; Wang, D. H.; Luo, C.; Cao, Y.; Nguyen, T.-Q.; Bazan, G. C.; Heeger, A. J. Effects of Solvent Additives on Morphology, Charge Generation, Transport, and Recombination in Solution-Processed Small-Molecule Solar Cells. *Adv. Energy Mater.* **2014**, *4*, 1301469.

(8) Wakioka, M.; Ishiki, S.; Ozawa, F. Synthesis of Donor–Acceptor Polymers Containing Thiazolo[5,4-d]Thiazole Units via Palladium-Catalyzed Direct Arylation Polymerization. *Macromolecules* **2015**, *48*, 8382–8388.

(9) Chen, S.; Lee, K. C.; Zhang, Z.-G.; Kim, D. S.; Li, Y.; Yang, C. An Indacenodithiophene–Quinoxaline Polymer Prepared by Direct Arylation Polymerization for Organic Photovoltaics. *Macromolecules* **2016**, *49*, 527–536.

(10) Hendriks, K. H.; Li, W.; Heintges, G. H. L.; van Pruissen, G. W. P.; Wienk, M. M.; Janssen, R. A. J. Homocoupling Defects in Diketopyrrolopyrrole-Based Copolymers and Their Effect on Photovoltaic Performance. *J. Am. Chem. Soc.* **2014**, *136*, 11128–11133.

(11) Pirotte, G.; Verstappen, P.; Vanderzande, D.; Maes, W. On the "True" Structure of Push–Pull-Type Low-Bandgap Polymers for Organic Electronics. *Adv. Electron. Mater.* **2018**, *4*, 1–12.

(12) Vangerven, T.; Verstappen, P.; Drijkoningen, J.; Dierckx, W.; Himmelberger, S.; Salleo, A.; Vanderzande, D.; Maes, W.; Manca, J. V. Molar Mass versus Polymer Solar Cell Performance: Highlighting the Role of Homocouplings. *Chem. Mater.* **2015**, *27*, 3726–3732.

(13) Love, J. A.; Proctor, C. M.; Liu, J.; Takacs, C. J.; Sharenko, A.; van der Poll, T. S.; Heeger, A. J.; Bazan, G. C.; Nguyen, T.-Q. Film Morphology of High Efficiency Solution-Processed Small-Molecule Solar Cells. *Adv. Funct. Mater.* **2013**, *23*, 5019–5026.

(14) Abdelsamie, M.; Treat, N. D.; Zhao, K.; McDowell, C.; Burgers, M. A.; Li, R.; Smilgies, D.-M.; Stingelin, N.; Bazan, G. C.; Amassian, A. Toward Additive-Free Small-Molecule Organic Solar Cells: Roles of the Donor Crystallization Pathway and Dynamics. *Adv. Mater.* **2015**, *27*, 7285–7292.

(15) Vangerven, T.; Verstappen, P.; Patil, N.; D'Haen, J.; Cardinaletti, I.; Benduhn, J.; Van den Brande, N.; Defour, M.; Lemaur, V.; Beljonne, D.; et al. Elucidating Batch-to-Batch Variation Caused by Homocoupled Side Products in Solution-Processable Organic Solar Cells. *Chem. Mater.* **2016**, *28*, 9088–9098.

(16) Müller, C.; Ferenczi, T. A. M.; Campoy-Quiles, M.; Frost, J. M.; Bradley, D. D. C.; Smith, P.; Stingelin-Stutzmann, N.; Nelson, J. Binary Organic Photovoltaic Blends: A Simple Rationale for Optimum Compositions. *Adv. Mater.* **2008**, *20*, 3510–3515.

(17) Defour, M.; Van den Brande, N.; Van Lokeren, L.; Van Assche, G.; Maes, W.; Vanderzande, D.; Van Mele, B. Influence of the Amorphous Phase and Preceding Solution Processing on the Eutectic Behaviour in the State Diagram of P3HT:PC61BM Determined by Rapid Heat–Cool Calorimetry. *RSC Adv.* **2016**, *6*, 92981–92988.

(18) Van den Brande, N.; Patil, N.; Guizar-Sicairos, M.; Claessens, R.; Van Assche, G.; Breiby, D. W.; Van Mele, B. Probing the Bulk Heterojunction Morphology in Thermally Annealed Active Layers for Polymer Solar Cells. *Org. Electron.* **2017**, *41*, 319–326.

(19) Van den Brande, N.; Van Assche, G.; Van Mele, B. Fast Scanning Chip Calorimetry Study of P3HT/PC61BM Submicron Layers: Structure Formation and Eutectic Behaviour. *Polym. Int.* **2019**, *68*, 277–282.

(20) Demir, F.; Van den Brande, N.; Van Mele, B.; Bertho, S.; Vanderzande, D.; Manca, J.; Van Assche, G. Isothermal Crystallization of P3HT:PCBM Blends Studied by RHC. *J. Therm. Anal. Calorim.* **2011**, *105*, 845–849.

(21) Heckler, I.; Kesters, J.; Defour, M.; Madsen, M.; Penxten, H.; D'Haen, J.; Van Mele, B.; Maes, W.; Bundgaard, E. The Influence of Conjugated Polymer Side Chain Manipulation on the Efficiency and Stability of Polymer Solar Cells. *Materials.* **2016**, *9*, 181.

(22) Brebels, J.; Kesters, J.; Defour, M.; Pirotte, G.; Van Mele, B.; Manca, J.; Lutsen, L.; Vanderzande, D.; Maes, W. A PCPDTTPD-Based Narrow Bandgap Conjugated Polyelectrolyte for Organic Solar Cells. *Polymer.* **2018**, *137*, 303–311.

(23) Koningsveld, R.; Stockmayer, W.H.; Nies, E. *Polymer Phase Diagrams: A Textbook*; Oxford University Press: Oxford, U.K., 2001.

(24) Danley, R. L.; Caulfield, P. A.; Aubuchon, S. R. A Rapid-Scanning Differential Scanning Calorimeter. *Am. Lab.* **2008**, *41*, 9–11.

(25) Wouters, S.; Demir, F.; Beenaerts, L.; Van Assche, G. Calibration and Performance of a Fast-Scanning DSC—Project RHC. *Thermochim. Acta* **2012**, *530*, 64–72.

(26) Prigogine, I.; Defay, R. *Chemical Thermodynamics*; translated D.H. Everett, Longmans Green: London, U.K., 1954.

TOC Graphic

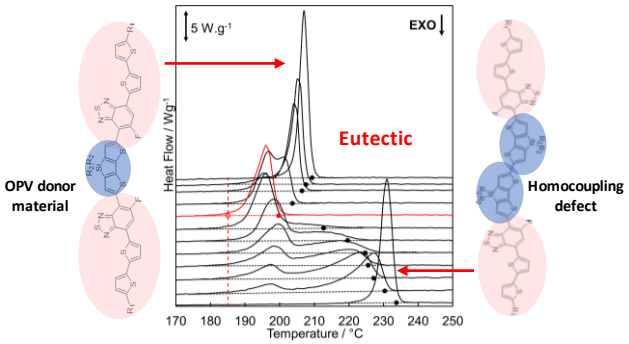
OPV donor material
5 W.g-1
EXO
Heat Flow / W.g-1
Eutectic
Homocoupling defect
170 180 190 200 210 220 230 240 250
Temperature / °C